Eur. J. Mineral.
2004, **16**, 877-889

Shear deformation experiments of forsterite at 11 GPa - 1400°C in the multianvil apparatus

HÉLÈNE COUVY[1, 2], DANIEL J. FROST[1], FLORIAN HEIDELBACH[1], KRISZTIÁN NYILAS[3], TAMÁS UNGÁR[3], STEPHEN MACKWELL[1,*] and PATRICK CORDIER[2,**]

[1]Bayerisches Geoinstitut, Universität Bayreuth, Germany
[2]Laboratoire de Structure et Propriétés de l'Etat Solide, UMR CNRS 8008, Université des Sciences et Technologies de Lille, Villeneuve d'Ascq, France
[3]Department of General Physics, Eötvös University Budapest, H-1445 Múzeum krt. 6-8, Budapest VIII, P.O.B. 323, Hungary

Abstract: Synthetic forsterite samples were shear-deformed at 11 GPa, 1400°C in the multianvil apparatus. The deformation microstructures have been characterised by SEM, EBSD, X-ray diffraction peak broadening and strain anisotropy analysis, and TEM. Different time durations have been characterised with a view to follow the evolution of strain and stress in high-pressure deformation experiments. A high density of [001] dislocations is introduced during pressurization at room temperature although no significant macroscopic shear or crystal preferred orientations are induced at this stage. The deviatoric stress is probably on the order of 1.5 GPa. Heating at 1400°C leads to a rapid decrease of the density of these dislocations. The shear deformation at high-temperature leads to measurable strain and development of crystal preferred orientations after one hour. Stress and strain-rate continue to decrease with time, such that eight hour experiments exhibit microstructures where recovery is apparent. At this stage, the stress level is estimated at *ca*. 100 MPa from dislocation density measurements. Crystal preferred orientations and TEM characterisation show that glide of [001] dislocations on (100) or (010) is the dominant deformation mechanism. Further investigation is needed to determine whether inhibition of [100] glide in these experiments is due to the role of water or whether a physical effect of pressure is also contributing.

Key-words: shear deformation, high-pressure, forsterite, dislocations, core structure.

1- Introduction

Olivine is by far the most abundant mineral of the upper mantle. It is also considered to be the weakest phase and hence to control the rheology of the upper mantle. For this reason, it has been clear for a long time that modelling the nature of convection in the outer 400 km of the Earth's mantle requires a good knowledge of the plastic properties of olivine. Many studies have been conducted to investigate the deformation mechanisms and flow laws of olivine single crystals (Blacic & Christie, 1973; Kohlstedt & Goetze, 1974; Durham & Goetze, 1977a and b ; Darot, 1980; Darot & Gueguen, 1981; Mackwell *et al*., 1985; Bai *et al*., 1991; Bai & Kohlstedt 1992a and b, 1993) and polycrystals (*e.g*., Chopra & Paterson, 1981, 1984; Karato *et al*., 1986; Hirth & Kohlstedt, 1995a and b; Mei & Kohlstedt, 2000a and b). Bai *et al*. (1991) and Bai & Kohlstedt (1992a and b) have shown that flow laws in olivine can be described by an equation of the form:

$$\dot{\varepsilon} = A\sigma^n f_{O_2}^m a_{opx}^q \exp(-\Delta H / RT) \quad (1)$$

where A is a constant for each particular slip system. This equation shows that the creep rate $\dot{\varepsilon}$ exhibits a dependence on stress (exponent n), oxygen fugacity (exponent m) and orthopyroxene activity (exponent q). Olivine is found to deform mostly along [001] (on (100) and (010)) at low temperature and high stress whereas [100] glide (on (010), (021), (031) and (001)) dominates at high temperature (and low stress). Although a wide range of thermochemical environments have been considered in the past, the physical conditions investigated remained quite narrow (mostly 1 atm pressure and high-temperature). Only recently has the influence of large strains (Bystricky *et al*., 2000; Zhang *et al*., 2000) and high-pressure (Karato & Rubie, 1997; Jung & Karato, 2001; Li *et al*., 2003, 2004; Raterron *et al*., 2003) been considered. Pressure has been shown to have a strong influence on the point defect chemistry (and hence on rheology) under "wet" conditions (Mackwell *et al*., 1985, Mei & Kohlstedt, 2000a and b; Jung & Karato, 2001). Experiments performed on olivine powders at 8 GPa and temperatures to 1475 K in a multianvil apparatus have

*E-mail: presently at : Lunar and Planetary Institute, 3600 Bay Area Blvd, Houston, TX 77058-1113, USA
**Patrick.Cordier@univ-lille1.fr

0935-1221/04/0016-0877 $ 5.85
DOI: 10.1127/0935-1221/2004/0016-0877

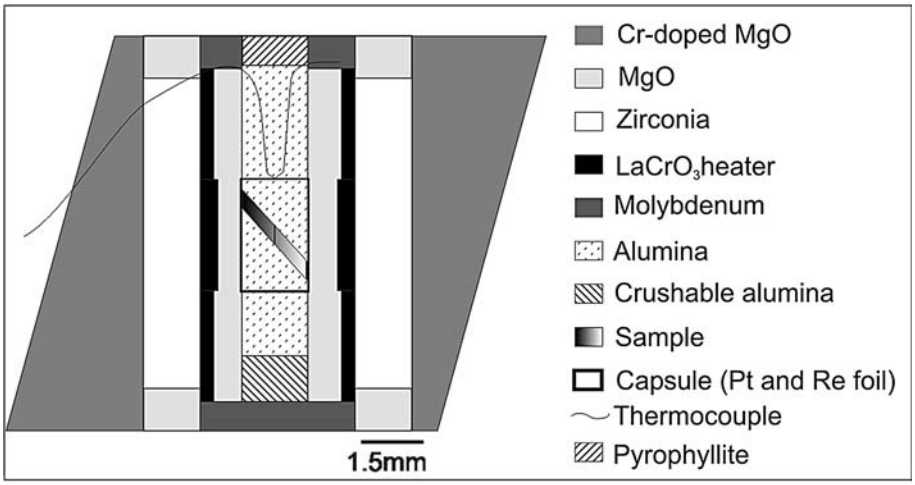

Fig. 1. Schematic of the high-pressure shear deformation assembly (after Karato & Rubie 1997).

emphasised the importance of dynamic recrystallization under these conditions (Li *et al*., 2003). However, elementary deformation mechanisms (slip system,…) and rheology of olivine at high pressure are still insufficiently documented.

Deformation experiments can now be achieved at pressures as high as 25 GPa (uppermost lower mantle) based on a modification of multi-anvil experiments (Cordier & Rubie, 2001). These experiments have been used to investigate the plasticity of the high-pressure polymorphs of olivine, wadsleyite (Fujimura *et al*., 1981; Bussod *et al*., 1993; Dupas *et al*., 1994; Sharp *et al*., 1994; Weidner *et al*., 1994; Ando *et al*., 1997; Chen *et al*., 1998; Dupas-Bruzek *et al*., 1998; Thurel & Cordier, 2003; Thurel *et al*., 2003a, b) and ringwoodite (Karato *et al*., 1998; Thurel, 2001). However, only limited attention has been paid so far to the deformation of olivine under lowermost upper mantle conditions (Li *et al*., 2003).

It is the aim of the present paper to address the question of the plasticity of olivine at high (11 GPa) pressure and 1400°C. We use the shear deformation assembly developed by Karato & Rubie (1997) in a multianvil apparatus. The deformation microstructures of the recovered specimens are characterised by electron backscattering diffraction (EBSD) in the scanning electron microscope (SEM), X-ray diffraction peak broadening and transmission electron microscopy (TEM). This characterisation provides information on the deformation mechanisms from the microscopic scale of the dislocation to the mesoscopic scale of dislocation densities and the macroscopic scale of the aggregate (crystallographic preferred orientations - CPO).

2- Experimental techniques

2-a Shear deformation in the multianvil apparatus

High-pressure experiments have been performed at the Bayerisches Geoinstitut in a 1200 tonne, MA-8 type, multi-anvil apparatus. These high-pressure deformation experiments require a two step procedure. First of all, a solid cylinder of forsterite is hot-pressed from Mg_2SiO_4 powder in a standard 18/11 (octahedral edge length / truncation edge length) high-pressure cell assembly at 5GPa and 1100°C for 4 hours. After hot-pressing, the dense specimens exhibit a fairly uniform grain size of 10-15 μm. The starting materials for the deformation experiments are thin (200 μm) slices cut at 45° from this cylinder. A second vertical cut is made dividing the specimen in two and the two exposed surfaces are coated with platinum to provide a strain marker. The specimen is then placed in an 18/11 version of the shear-deformation assembly designed by Karato & Rubie (1997). In this assembly, the forsterite sample is sandwiched between two hard alumina pistons cut at 45° (Fig. 1). Plastic strain is obtained during heating from the relaxation of stresses accumulated during compression. The sample is thus deformed in a shear configuration. In our set-up, the strain marker is parallel to the axis of the furnace in order to record sample shear only, with no contribution of compaction. Deformation experiments were performed at 11 GPa and 1400°C. The temperature was calibrated with the enstatite-diopside thermometer (Nickel *et al*., 1985). The temperature gradient across the sample is less than 50°C at a nominal temperature of 1400°C. The only variable parameter in this study is the heating time duration (Table 1). For each time duration, several experiments have been performed to test the reproducibility of the strain and of the microstructures. Some specimens have been compressed and not heated to characterise possible cold deformation during pressurisation. Three different time durations at temperature have been investigated: one minute, one hour and eight hours. After deformation, the samples are recovered and prepared for microstructural characterisation. Two different kinds of specimens have been made: cross sections and plane views (parallel to the specimen slice).

Table 1. Experimental conditions for forsterite deformation in the multianvil apparatus.

Run #	Sample # Hot-pressed	Oil pressure (bar)	Nominal pressure (GPa)	Temperature (°C)	Duration (min)	Strain marker rotation (deg.)	Piston displacement (μm)	
S2964	S2911	360	11	1400	-	6 (4)	80 (10)	Not heated
S2970	S2947	360	11	1400	-	9 (3)	89 (10)	Not heated
S3024	S3017	360	11	1400	-	10 (11)	200 (40)	Not heated
S2996	S2961	360	11	1400	1	9 (3)	93 (30)	
S2997	S2961	360	11	1400	1	10 (4)	93 (50)	
S2917	S2897	360	11	1500	60	5 (3)	119 (20)	
S2954	S2910	360	11	1400	60	8 (2)	142 (40)	Quenched over in 3min
S2955	S2911	360	11	1400	60	13 (5)	145 (20)	Quenched over in 10 min
S2993	S2947	360	11	1400	60	11 (6)	123 (30)	
S2994	S2961	360	11	1400-1500	60	6 (2)	137 (40)	TC uncertain
S2984	S2947	360	11	1400	480	15 (8)	133 (20)	
S2998	S2897	360	11	1400	480	8 (4)	100 (20)	
S3079	S3017	360	11	1400	480	13 (14)	77 (20)	

Specimen numbers # correspond to hot pressing experiments carried out at 5 GPa, 1100°C for four hours. Strain marker rotation and piston displacements recorded after deformation, and error margin due to sample preparation.

2-b X-ray diffraction peak broadening analysis and evaluation of strain anisotropy

X-ray diffraction peak broadening analysis

Dislocations are characterised by a long-range strain field causing a peak broadening of the fundamental Bragg reflections. Conventional peak profile analysis methods of Williamson & Hall (1953) and Warren & Averbach (1950) have been upgraded by taking into account the contrast effect of dislocations on peak broadening (Ungár & Borbély, 1996). The contrast factor, *C*, is a function of the *hkl* indices of the reflection, the Burgers- and line vectors of the dislocations, $\boldsymbol{b}$ and $\boldsymbol{l}$, and the elastic constants of the crystal in a similar way as in TEM. C is thus characteristic for a given slip system. The anisotropic contrast effect of dislocations has been used to model the strain anisotropy observed on X-ray diffraction profiles of cubic and hexagonal crystals (Ungár *et al*., 1999; Ungár & Tichy, 1999; Ungár *et al.*, 2001). Here the technique has been extended to orthorhombic crystals. This technique has the advantage over TEM in that it provides information on a large number of dislocations that are more statistically relevant and it can be applied to high dislocation densities, *e.g.* 10^{18} m^{-2}. Besides the *modified* Williamson-Hall and Warren-Averbach methods (Ungár *et al*., 2001) whole profile fitting procedures (Ribárik *et al*., 2001 and 2004) have been developed and used here for the determination of the experimental values of dislocation contrast factors.

The specimens were cut as in Fig. 2b. Consequently, the forsterite is surrounded by alumina and contains some Pt. Three windows have been found in the entire diffraction angle range where only the reflections of forsterite are present. In these three windows the profiles of five reflections have been investigated: (021), (101), (002), (130), (220). Monochromatic Cu$K\alpha$ radiation from a fine focus rotating anode (Nonius FR 521), operated at 40 kV, 70 mA was used. The footprint of the beam on the specimen was 0.1 x 0.8mm. The diffraction profiles were registered by a linear position sensitive gas filled detector (OED 50 Braun, Munich) at a distance of 140 mm from the specimen. The linear resolution of the detector is about 80 μm. The specimen was mounted on a two axis standard crystallographic goniometer-head with additional x-y translations in the horizontal plane in order to move the specimen within the X-ray beam with high precision.

Evaluation of strain anisotropy

Strain anisotropy in X-ray line-profile analysis means that neither the full-width at half maximum (FWHM) nor the integral breadths nor the Fourier coefficients in the Warren-Averbach plot are monotonous functions of the diffraction vector or its square, $\boldsymbol{g}$ or $\boldsymbol{g}^2$. It can be rationalised by the dislocation contrast factors, *C*, which, on the other hand provide useful further information on the dislocation structure of the specimen (Wilkens, 1970; Ungár & Borbély, 1996; Ungár *et al*., 2001). If all possible slip systems are randomly populated or if the specimen is more or less texture free the contrast factors corresponding to the same *hkl* indices can be averaged over the permutations of the indices (Ungár & Tichy, 1999). Since the specimen is a fine grained polycrystal, these average contrast factors can be used. For cubic and hexagonal crystals the numerical parameters in the average contrast factor formula are well understood (Ungár & Tichy, 1999; Dragomir & Ungár;

2002). For orthorhombic crystals the average contrast factors are:

$$\bar{C} = \alpha + \beta[(h^4+a_1k^4+a_2l^4+a_3h^2k^2+a_4h^2l^2+a_5l^2k^2)/(h^2/a^2+k^2/b^2+l^2/c^2)^2], \quad (2)$$

where a, b and c are the lattice constants, h, k and l are the Miller indices and a_i, i = 1-5 are numerical constants depending on the dislocation type and the elastic constants of the crystal. α and β are auxiliary constants which influence only the absolute value of , but do not influence the *hkl* dependence of it (Ungár *et al*., 2001). The average contrast factors for orthorhombic crystals are calculated numerically by using the general formula for contrast factors (Klimanek & Kuzel, 1988; Ungár & Tichy, 1999). The physical interpretation of the a_i constants in terms of different dislocation types and/or elastic constants is, however, not yet available. In the present case, the a_i numerical constants are determined by fitting the FWHM of the five measured profiles according to the *modified* Williamson-Hall equation, (*c.f*., Eq (9) in Ungár *et al*., 2001). From the a_i values, obtained here, relative values of the contrast factors, $\bar{C}$* were calculated. A large number of experiments (Wilkens, 1970; Ungár *et al*., 2001) have shown that the approximate mean of the average contrast factors is : $<\bar{C}> \cong 0.4$. The mean of the $\bar{C}$* values were adjusted accordingly. With these calculated and adjusted $\bar{C}$ values the dislocation densities are calculated by using the *multiple whole profile* (MWP) fitting procedure that applies physically well established profile functions for the size and strain profiles, respectively (Ribárik *et al*., 2001).

2-c SEM, EBSD and TEM

Cross-sections and planar sections of the whole samples were imaged with an SEM in order to examine the grain size and shape as well as to measure the strain marker rotation. The texture analysis was performed with an SEM using the EBSD technique (Dingley, 1984). Through automation of the procedure (Adams *et al*., 1993), the microstructure and texture at the sample surface can be mapped. From these measurements, pole figures are derived showing the orientation of each crystal axis relative to the sample coordinates. The discrete point distributions are converted into densities by grouping them within a 5° area and then smoothing with a Gaussian function with a 15° FWHM. The resulting density distributions are normalised and contoured.

EBSD requires a high crystallographic quality of the analysed surface layers. A final polishing with colloidal silica suspension was performed in order to remove the shallow layers damaged by mechanical grinding. All the SEM measurements were performed with a Leo Gemini 1530 SEM equipped with a field emission gun (FEG) and an EBSD detector. The parameters of the beam for imaging and for measurements are an accelerating voltage of 20 kV, a working distance of *ca*. 20 mm and a probe current of 3.5 nA. Automated indexing and pole figure construction were performed with the software CHANNEL (HKL Technology).

Doubly polished thin (25 μm) sections have been prepared from the recovered specimens for TEM observation. The samples have been glued on a Mo grid and ion milled at 5 kV under a low beam angle of 15° until electron transparency is reached. TEM observations were carried out in Lille with both a Philips CM30 microscope operating at 300 kV and a 200 kV Jeol 200CX and in Bayreuth on a Philips CM20 FEG microscope.

2-d Infrared spectroscopy

Infrared spectra were measured using a Bruker IFS 120 HR high-resolution Fourier-transform spectrometer. Measurements were carried out using a tungsten light source, a CaF_2 beam-splitter and a high-sensitivity, narrow-band MCT detector. Two hundred scans were accumulated for each spectrum. During the measurement, the optics of the spectrometer were evacuated and the microscope was purged with a stream of H_2O- and CO_2-free purified air. We used a spot size of 100 μm allowing several grains to be measured together. Unpolarized Fourier transform infrared (FTIR) spectra were obtained at room temperature on 100 μm thick polished sections. To determine the concentration of hydroxyl groups in the deformed samples, the infrared spectra were integrated from approximatively 3625 to 3300 cm^{-1}, the region dominated by the stretching vibrations due to the OH bonds. The integration was carried out using the calibration from Paterson (1982).

3- Results

Figure 2a presents a cross section of a high-pressure shear deformation assembly which has been compressed to 11 GPa. An enlargement of the sample capsule is displayed in Fig. 2b which shows the displacement of the upper piston with respect to the lower piston. The strain marker is visible in Fig. 2c. Note that it was vertical prior to the experiment.

3-a Strain marker rotation and piston displacement

The rotation of the strain marker is used to evaluate the total shear deformation undergone by the specimen. In these experiments, the strain marker is placed parallel to the axial compression so as not to record a possible compression of the specimens. We have, however, found compression to be negligible in our experiments (no measurable change in the sample thickness). The values for the strain marker rotation measured for all the experiments are presented Table 1. They show that in all cases the strain marker rotation is small, probably lower than 10°. Indeed, specimens that were compressed but not heated exhibit a non-zero rotation between 6 and 10°. No significant evolution is found between "one minute" and "eight hour" experiments. Following the same trend, the piston displacement is not found to evolve significantly with time passed at high-temperature. Altogether, these measurements suggest that the total shear strain undergone by the forsterite specimens deformed at 11GPa, 1400°C is probably below $\gamma = 0.3$.

3-b SEM and EBSD

Figure 3 presents typical microstructures at various stages as seen using the SEM. The starting material (after hot pressing) is shown in Fig. 3a. It consists of equilibrated grains with a mean size of 10 µm. After cold compression (Fig. 3b), the overall microstructure is unchanged although most grains exhibit significant damage (cracks) due to the application of deviatoric stress (see enlargement of Fig. 3b). This distortion is no longer visible after only one minute at 1400°C (Fig. 3c). For longer time durations (one and eight hours: Fig. 3d-e), the only visible modification is a slight increase in the grain size (Fig. 4).

These results of EBSD characterisation are presented in Fig. 5. The hot-pressed specimen shows no CPO. The same conclusion holds for specimens cold-compressed and annealed for one minute. Only after one hour can we distinguish some CPO, although it remains weak. The [001] pole figures show point maxima close to the shear direction (X_0). In most cases, we observe an alignment of [100] directions with the shear plane normal (Y_0). In some cases however (S2955 and S2994), we observe one [010] directions clustering around (Y_0) still with alignment of [001] directions close to the shear direction (X_0). An exception is S2993 which shows no comprehensive CPO. All the CPOs observed after one hour appear to weaken for longer time durations (eight hours).

3-c X-ray peak broadening

Typical peak profiles of the 101 reflections as a function of the duration of the experiment are shown in Fig. 6. It can be seen that the "null test" specimen reveals the largest broadening in accordance with the fact that it was compressed at room temperature but not heated. The peak broadening decreases with holding time at high temperature. The FWHM of the five investigated reflections are shown in the classical Williamson-Hall plot in Fig. 7 as a function of d* ($d^* = 2sin\theta/\lambda$, where θ is the diffraction angle and λ the wavelength of the X-rays). The strongly non-monotonous behaviour of the values of the FWHM indicates a pronounced strain anisotropy. Using the average dislocation contrast factors, as described in 2-b above, the *modified* Williamson-Hall plot can be constructed as shown for four different specimens in Fig. 8. It can be seen that, within experimental error, the strong strain anisotropy is well rationalized by the dislocation model of strain. For example, the full diamonds or the crosses scatter strongly versus d* in Fig. 7, whereas in Fig. 8 they follow straight lines within the experimental error. The very different slopes of the straight lines fitted to the data points indicate large differences in the lattice strains in the different specimens, the larger slope indicates more strain. The dislocation structure can only be characterised by at least two parameters, the density and the arrangement of dislocations, ρ and M, where $M = R_e\rho^{1/2}$ and R_e is the effective outer cut-off radius of dislocations. In the case of narrow dislocation dipoles with strong screening of mutual strain fields R_e is smaller than the average dislocation distance, and M is smaller than unity. With such dislocation arrangements the diffraction profiles have long tails.

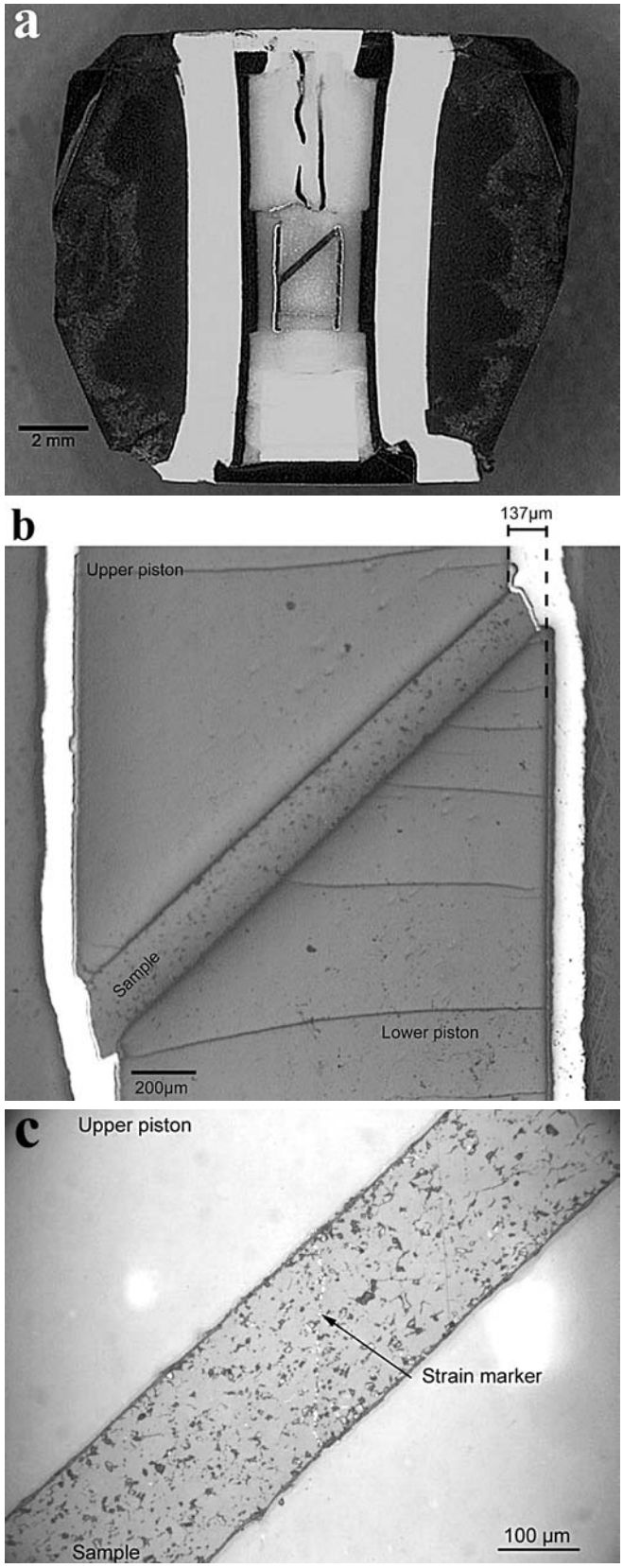

Fig. 2. Optical micrographs of high-pressure cells after deformation.
Cross section of the octahedron. Sample S2970.
Enlargement of the sample capsule. Note the piston displacement on both sides. Sample 2994.
Central part of the specimen showing the strain marker. Sample S2997.

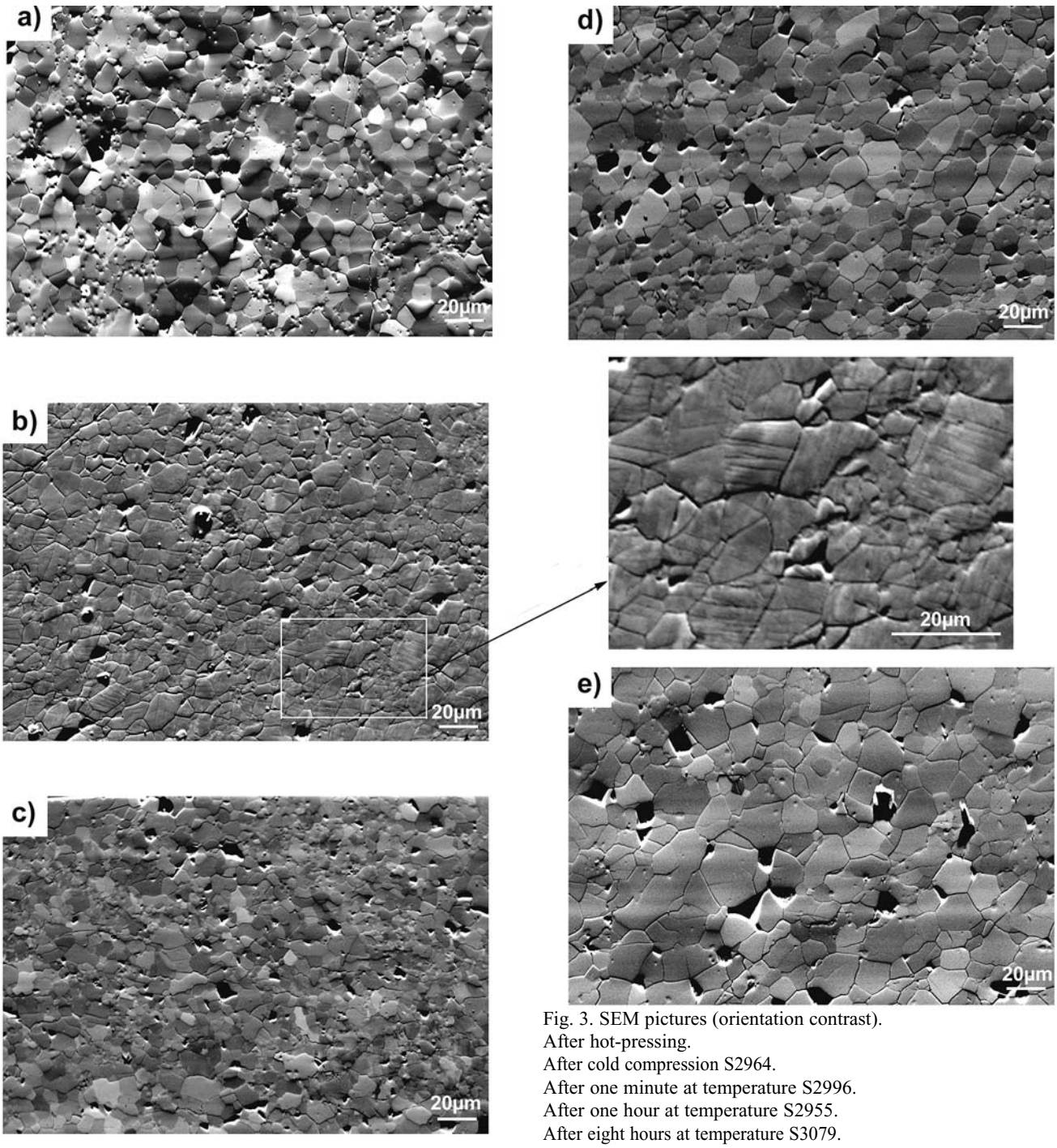

Fig. 3. SEM pictures (orientation contrast).
After hot-pressing.
After cold compression S2964.
After one minute at temperature S2996.
After one hour at temperature S2955.
After eight hours at temperature S3079.

In the opposite case, *i.e.* wide dislocation dipoles, with weak screening and M larger than unity, the diffraction profiles are bell shaped. The slope alone in the *modified* Williamson-Hall plot can certainly not provide the two parameters, ρ and M. The whole profile, however, is not only broadened but its shape is also influenced by dislocation structure. Therefore, the breadth and the profile shape in a whole profile analysis enable to determine the two parameters, ρ and M, simultaneously (*cf.* Wilkens, 1970). The MWP fitting method provides also crystallite size parameters in terms of the median and the variance, m and σ, of the log-normal size distribution function. The X-rays give the size of the coherently scattering domain: this is the *smallest undisturbed volume* in the crystal, this need not be the grain size which is visible *e.g.* in a TEM micrograph. From m and σ the area average mean crystallite diameter, $\langle x \rangle_{area}$, can be calculated as (Hinds 1982):

$$\langle x \rangle_{area} = m \exp(2.5\sigma^2) . \quad (3)$$

The size parameters and the dislocation densities in the different specimens are listed in Table 2. The dislocation densities found with this method are in good agreement with the few densities measured on TEM micrographs.

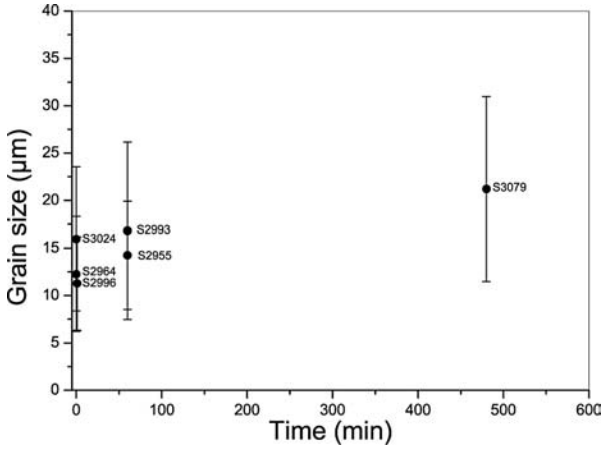

Fig. 4. Evolution of the grain size with time at 1400°C. The grain size was measured by the software ImageTool, which calculates the area of each grain from a redrawn SEM picture. It determines the diameter corresponding to a circle having the same area. Bars represent data scattering (2σ standard deviation).

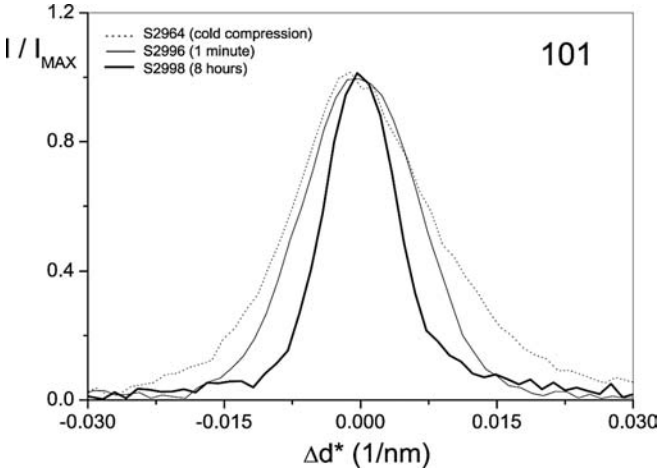

Fig. 6. Typical profiles of the 101 Bragg peaks in three different specimens. The decrease of peak width with annealing time can be observed.

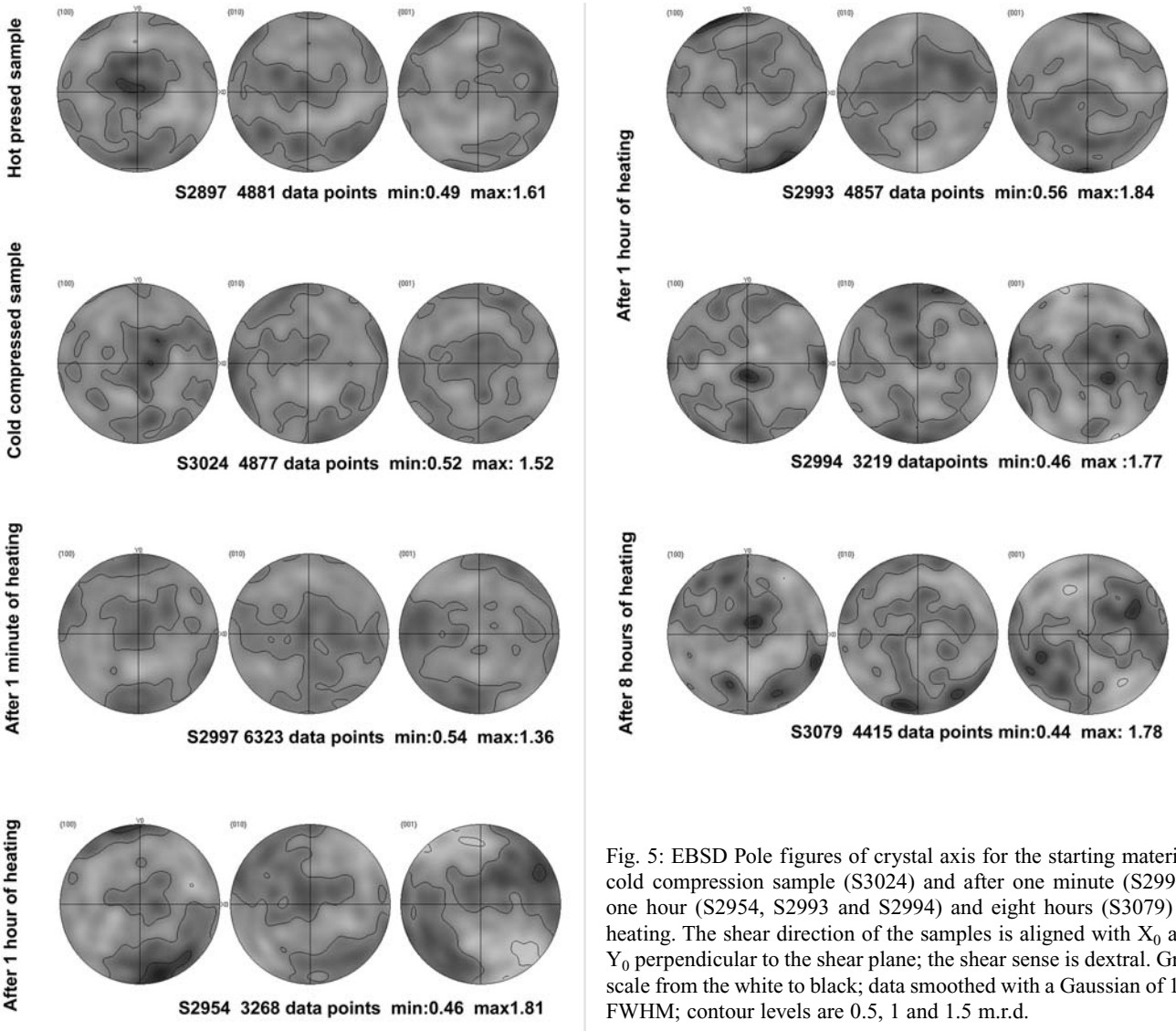

Fig. 5: EBSD Pole figures of crystal axis for the starting material, cold compression sample (S3024) and after one minute (S2997), one hour (S2954, S2993 and S2994) and eight hours (S3079) of heating. The shear direction of the samples is aligned with X_0 and Y_0 perpendicular to the shear plane; the shear sense is dextral. Gray scale from the white to black; data smoothed with a Gaussian of 15° FWHM; contour levels are 0.5, 1 and 1.5 m.r.d.

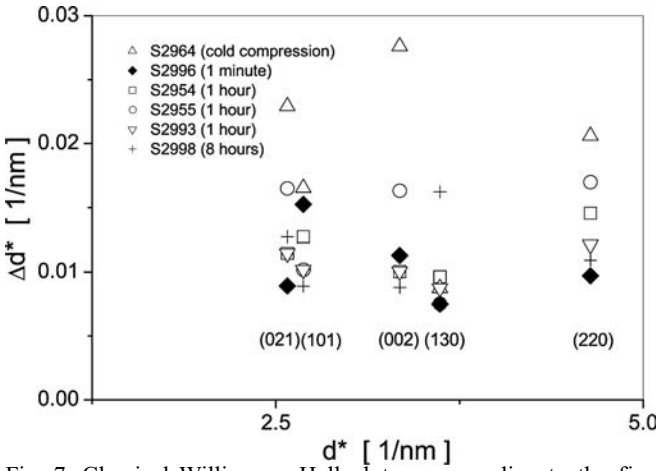

Fig. 7. Classical Williamson-Hall plot corresponding to the five investigated forsterite reflections

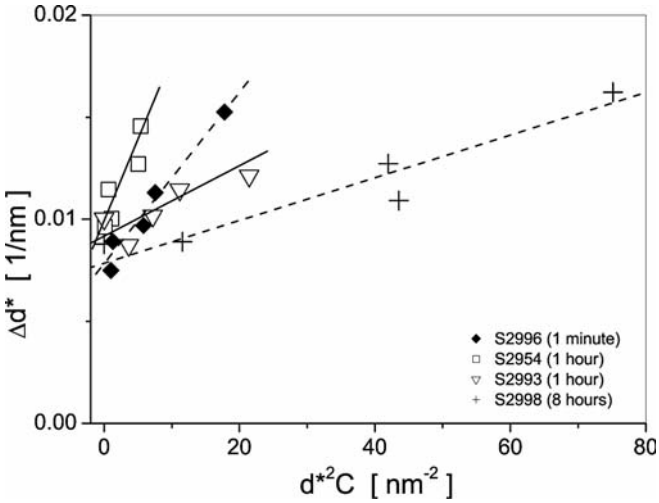

Fig. 8. *Modified* Williamson-Hall plot corresponding to the five investigated forsterite reflections (For the sake of clarity only 4 typical specimens are shown).

3-d TEM

All the specimens analysed using the TEM are characterised by the pervasive occurrence of [001] dislocations although the microstructures are found to evolve significantly with time duration at high-temperature. After cold compression, all grains contain high densities of dislocations, as already determined by X-ray peak broadening. These dislocations, with [001] Burgers vectors, exhibit marked line orientations along edge and screw directions (Fig. 9a) characteristic of a high lattice friction on both characters. Very comparable microstructures are observed in specimens heated for one minute although the density of edge segments begins to decrease. After one hour, the microstructure of each grain is dominated by straight screw [001] dislocations (Fig. 9b). One can also find in these specimens widely dissociated dislocations (Fig. 9c). In specimens annealed for eight hours, most grains are pristine. Some grains, however, still contain [001] screw dislocations in addition to some subgrain boundaries (Fig. 9d).

3-e Infrared results

The results of the infrared measurements are presented in Table 3. It appears from these measurements that every sample originally contains hydroxyl at the thousands H/10^{6}Si scale. It also appears that this hydroxyl content is heterogeneous. Despite this heterogeneity, Table 3 shows a trend suggesting that the hydroxyl content decreases with times spent at high temperature to reach a level of a few hundreds of H/10^{6}Si after 8 hours.

4- Discussion

4-a Evolution of deformation with time

In this study, we have, for the first time, attempted to characterise the deformation history in a shear-deformation experiment performed in a multianvil apparatus. The main drawback of high-pressure deformation experiments based on anisotropic cell assemblies is that deformation and pressure are not independent variables. This has two consequences. The first is that the samples may undergo undesired plastic deformation during pressurisation at room temperature (Thurel *et al*., 2003a), although this has never been clearly demonstrated for the case of the shear-deformation assembly. The second consequence is that these experiments are comparable to relaxation tests with steadily decreasing stress and strain-rate. This is well illustrated by the evolution of the dislocation densities with time duration at high temperature (Fig. 10). Experiments S2964, S2970 and S3024 were designed to evaluate the influence of cold pressurisation on the sample. The TEM

Table 2. The median, m and the variance, σ of the crystallite size distribution function, the area averaged mean crystallite diameter, $\langle x \rangle_{area}$, and the average dislocation density, ρ.

Specimen	m [nm]	σ	$\langle x \rangle_{area}$ [nm]	ρ [10^{14} m^{-2}]
S2964 (cold compression)	55 (5)	0.38 (0.05)	80 (5)	16 (4)
S2996 (1 minute)	161 (10)	0.01 (0.01)	160 (10)	2.2 (0.5)
S2954 (1 hour)	94 (10)	0.19 (0.05)	105 (10)	2.2 (0.5)
S2955 (1 hour)	63 (5)	0.36 (0.05)	90 (5)	2.8 (0.5)
S2993 (1 hour)	118 (10)	0.06 (0.02)	120 (10)	0.04 (0.02)
S2998 (8 hours)	122 (10)	0.12 (0.05)	130 (10)	0.09 (0.02)

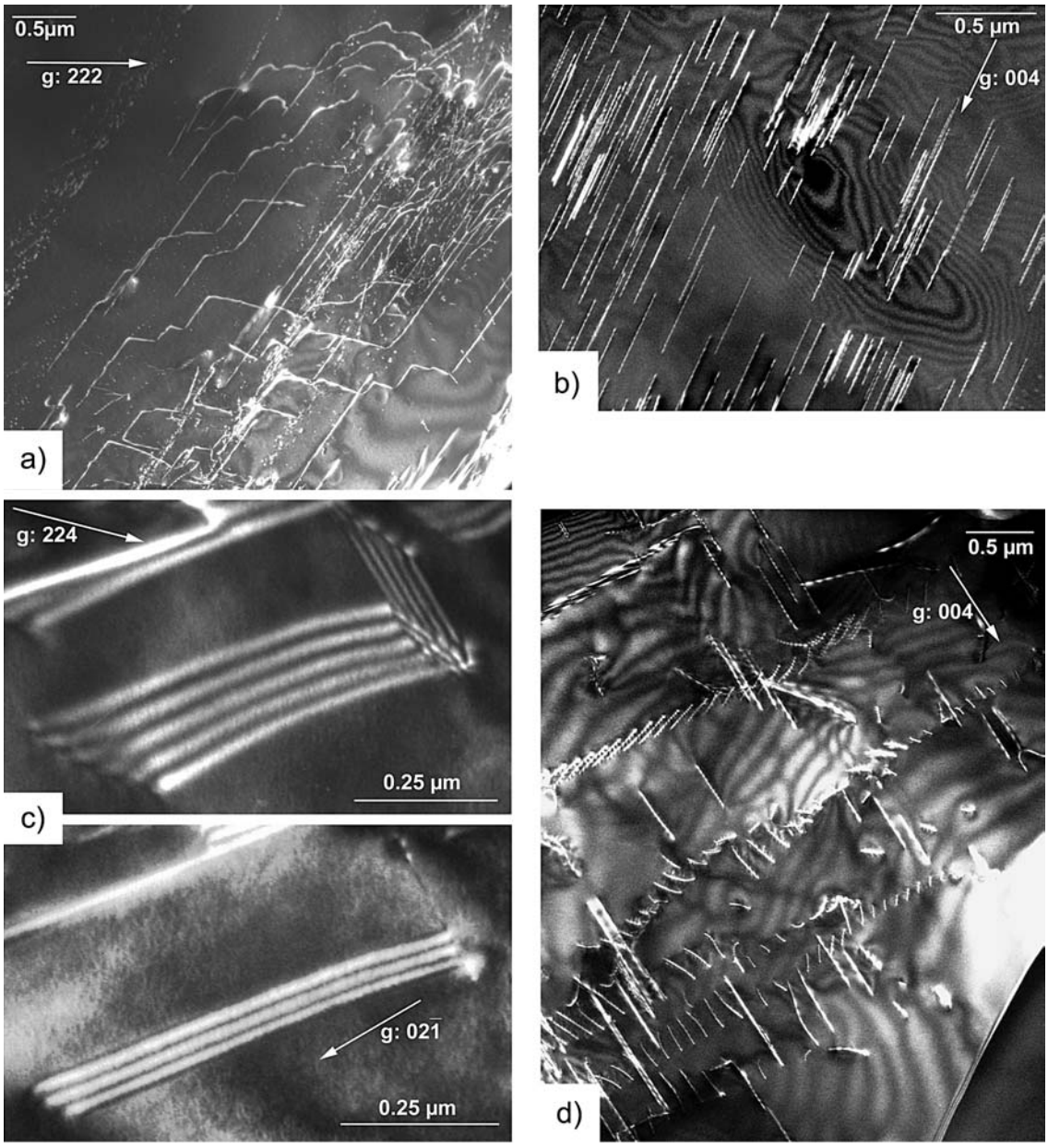

Fig. 9. TEM micrographs Weak-beam dark-field.
a) Sample S3024, cold compressed at 11 GPa and not heated. [001] dislocations in glide configuration. Note the abundant edge segments exhibiting lattice friction. g: 222.
b) Sample S2954, deformed for one hour at 11 GPa, 1400°C. [001] screw dislocations. g: 004.
c) Sample S2994, deformed for one hour at 11 GPa, 1400°C. Extended stacking faults.
Top: viewed inclined. g: 224.
Bottom: viewed edge-on. The stacking fault is parallel to (021). g: 021.
d) Sample S2984, deformed for eight hours at 11 GPa, 1400°C. Subgrain boundaries containing [001] dislocations. g: 004.

investigations as well as the dislocation density measurements by X-rays show that high stresses are imposed on the specimen during the pressure increase, resulting in dislocation densities of up to 1.6 10^{15} m^{-2}. However, this cold working does not correspond to measurable strains as shown by the minimal strain marker rotation and, more importantly, by the absence of a detectable CPO. TEM investigations show that deformation is produced by [001] glide. This could be expected as this deformation mecha-

Table 3. Hydroxyl content on specimens recovered after deformation, as measured using infrared spectroscopy.

Specimen	Hydroxyl content (H/10^6Si)
S3024 (cold compression)	1902 (884)
S2996 (1 minute)	1888 (276)
S2955 (1 hour)	2248 (468)
S2993 (1 hour)	853 (446)
S3078 (8 hours)	289 (34)

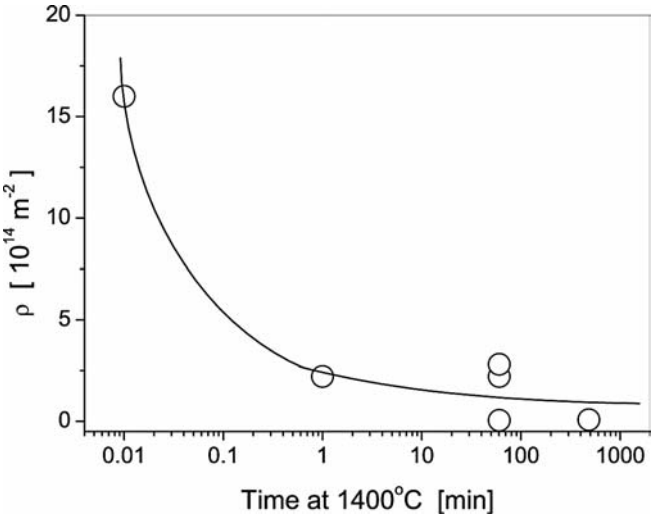

Fig. 10. Dislocation density as a function of duration at 1400°C. The open circle at 0.01 min corresponds to the "null test" specimen. The line is a guide for the eye.

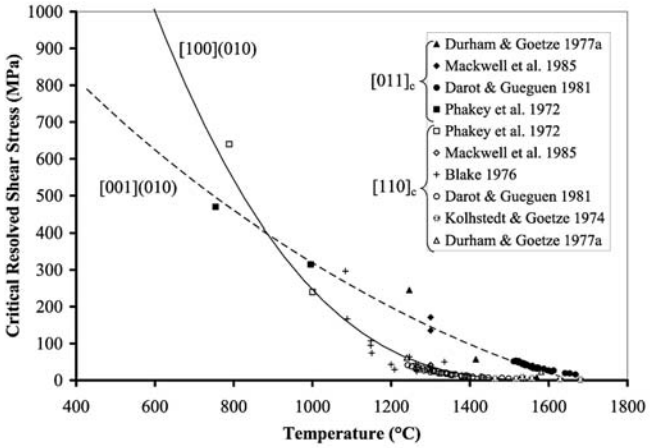

Fig. 11. Critical resolved shear stresses of [100](010) and [001](010) as a function of temperature. Data (corresponding to a strain-rate of $10^{-5}s^{-1}$) from experiments performed on single crystals oriented along $[011]_c$ (black-filled symbols) to promote [001](010) glide and along $[110]_c$ to promote [100](010) glide.

nism is known to be the easiest one at low temperature under high stresses. It is interesting to note, however, that both edge and screw segments are present with comparable densities. This demonstrates that, at room temperature, edge [001] dislocation segments bear a high lattice friction as do screw segments.

Experiments S2996 and S2997 correspond to a very short annealing time (one minute), and hence, mostly emphasise the influence of the temperature ramp, as temperature is raised to 1400°C in about 15 min in our experiments. The salient point is that the dislocation density dropped significantly during this stage. In particular, it is remarkable at the TEM that the number of edge segments is considerably reduced. As temperature is raised, the mobility of edge [001] dislocations becomes much higher than the mobility of screw segments. Meeting no obstacles, they glide until they annihilate at the grain boundaries. Observation of these specimens shows that the cold-working microstructure introduced during compression is largely recovered after only one minute at temperature (and temperature ramp of course). However, no texture (CPO) is produced at this stage. Although high, the density of dislocations introduced during cold compression was not sufficient to produce any CPO.

The total strain achieved after one hour of annealing is limited, as shown by the small rotation of the strain marker. Although this measurement is subject to some uncertainty, the strain is probably always less than 30 %. However, there is enough strain to produce weak CPO patterns. Five experiments have been carried out under these conditions. All but one (S2993) exhibit CPO's with marked alignment of [001] toward the shear direction, which is indicative of [001] slip. This conclusion is consistent with TEM observations which show dislocation microstructures dominated by straight screw [001] dislocations. In most cases, the CPO's point toward glide of [001] dislocations on (100), but S2955 and S2994 suggest rather slip on (010). This difference suggests that glide of [001] dislocations is as easy on (100) as on (010). The final CPO would thus be determined by the orientation distribution function of the starting materials. It is to be noted that no confirmation on the slip plane can be drawn from the TEM observations as the dislocation microstructures are dominated by screw segments only.

Much longer annealing times (8 hours) do not lead to significantly larger strains as shown from the strain marker and the CPOs. The CPOs are slightly weaker than after one hour, probably due to the influence of grain growth. At the microscopic scale, we find that dislocation activity is restricted to a few grains, certainly those that are favourably oriented. However, the microstructures are quite different with the advent of numerous subgrain boundaries. This observation suggests that the strain rate has decreased after 8 hours such that recovery effects (promoted by climb) become predominant. But, this decrease of the strain rate is not accompanied by any visible change of the deformation mechanism (activation of [100] glide for instance). The deformed grains still exhibit [001] screw dislocations only, as in the samples annealed for only 1hour.

One might derive an estimate of the effective stress (and of its evolution with time) during deformation from the dislocation densities (Kohlstedt & Weathers, 1980). Dislocation microstructures induced during cold compression point to relatively high stress levels of the order of 1.5 GPa. Heating results in rapid stress relief which is achieved when nominal temperature is reached. Then, the stress level remains fairly constant (within the uncertainties) of the order of a few hundreds MPa up to one hour. After 8 hours stress has decreased to *ca*. 100 MPa.

4-b Deformation mechanisms in olivine at 1400°C, 11 GPa

Our salient observation is the dominant role of [001] dislocations in our high-pressure experiments. The occurrence of [001] glide has been well documented in the past,

from room-pressure deformation studies of olivine single crystals (*i.e*. Darot & Gueguen, 1981; Kolhstedt & Goetze, 1974). The relative ease of [100] and [001] glide depend critically on temperature and strain-rate. Deformation experiments on oriented single crystals have been used to derive the Critical Resolved Shear Stress (CRSS) for dislocation glide on a particular slip system. As an illustration, Fig. 11 shows how the CRSS of [100] and [001] dislocations on (010) evolve with temperature at a strain-rate of $10^{-5}s^{-1}$. It is shown that slip along [001] is easier below a critical temperature, while [100] glide becomes easier at higher temperature. The influence of strain-rate is illustrated by dislocation microstructures found in shocked olivine (either in meteorites or from experiments, see for instance the recent review from Leroux 2001 and references herein) which are dominated by [001] dislocations.

Previous studies have already reported evidence for [001] glide under high-pressure conditions. For instance, [001] glide has recently been reported by Raterron *et al*. (2004) and Li *et al.* (2003) at 8-9 GPa and 500-890°C. But, in this temperature range, [001] glide would be expected, as illustrated by Fig. 11. Samples deformed at 15 GPa and 900°C for 30 min by Dupas-Bruzek *et al.* (1998) also contained remnant olivine grains with high densities of [001] dislocations. The same observation has recently been made in dry $(Mg,Ni)_2GeO_4$ olivine deformed at 300 MPa and 1200°C, in the $\alpha + \gamma$ stability field (Julian Mecklenburgh, pers. comm.). The occurrence of [001] glide in high-pressure experiments is usually attributed to the application of high stresses. It is to be noted, however, that the present situation (high-stresses at high temperature) cannot be compared easily with low-temperatures or shock experiments.

The detailed microstructural investigation performed in the present study was aimed at casting some light on this issue. We confirmed that very high stresses result from compression at room temperature and that many [001] dislocations are introduced at this stage. Heating the sample to 1400°C induces rapid stress relaxation and eliminates most of these defects without producing significant macroscopic strain (CPO). The CPO observed after one hour are thus the result of the nucleation and glide of dislocations at T = 1400°C under stress levels below *ca*. 500 MPa. The usual creep experiments suggest that [100] glide should have been activated at this temperature. The striking observation is not the occurrence of [001] slip, but the absence of [100] dislocations. Our results cannot be understood from the known CRSS of [100] and [001] glide presented in Fig. 11. We are thus lead to postulate either that [100] glide becomes so hard that it is inhibited, or that [001] glide is enhanced. The observation at the TEM that [001] dislocations still face high lattice friction rather suggests inhibition of [100] glide.

The origin for such behaviour is not clear at this point and we can only suggest a working hypothesis at present. The stress issue cannot be ruled out as we do not have enough information on the influence of this parameter at high-temperature on dislocation mobilities. Dislocation mobility changes might also result from the presence of dissolved hydroxyls as suggested by the results of Jung & Karato (2001) obtained at 2 GPa on water-bearing olivine. However, Jung & Karato's experiments lead to dislocation microstructures that are significantly different from ours, *i.e*. with [100] dislocations and [001] dislocations which no longer exhibit straight characters (Shun-ichiro Karato, pers. comm.). Certainly, water does play a role in our experiments, probably promoting grain boundary migration; but concerning dislocation mobility, the situation is less clear. Changes in dislocation mobility can also arise from a pressure-induced modification of the dislocation core fine structure. Such an effect of pressure on dislocation core structure has already been reported in Ta (Yang *et al*., 2001). This effect could be related to our observations of widely dissociated dislocations, which have never been reported, to the best of our knowledge, in low-pressure experiments. Indeed, the occurrence of climb dissociation has a dramatic effect on dislocation mobility (Bretheau *et al*., 1979). More theoretical work on the fundamentals of dislocation mobility in olivine (including the influence of stress, pressure,…) appears necessary to provide an explanation for this change in deformation mechanism.

5- Conclusion

Shear deformation experiments have been performed on forsterite aggregates in the multianvil apparatus at 11 GPa, 1400°C. In the absence of direct mechanical data, a detailed, multiscale, microstructural characterisation has been conducted for different experimental durations to understand how deformation proceeds with time in such experiments. It is found that cold pressurization induces high-stresses (estimated at around: 1.5 GPa), which introduce a high density of dislocations in the sample. Dislocation mobilities are not sufficient, however, to produce significant strain at this stage. This cold-working microstructure is rapidly (a few minutes) recovered as temperature is raised to 1400°C. Dislocation multiplication and mobility becomes sufficient to induce significant plastic shear as shown by the produced CPO's. The maximum plastic shear observed ($\gamma \approx 0.3$) is however smaller than in previous experiments (Karato & Rubie, 1997; Karato *et al*., 1998; Jung & Karato, 2001), although the deformation experiments are quite distinct. In our experiments, stress and strain-rate decrease rapidly during heating and then more slowly when temperature is held constant. As a result, the strongest CPO's have been obtained after heating for one hour. After eight hours, the strain-rate was probably very small and recovery processes became more important. The mechanical conditions are obviously complicated in this kind of experiment and require careful microstructural characterisation. It must be remembered however that multianvil shear deformation experiments represent one of the very few tools that enable plastic deformation experiments to be performed at the P, T conditions of the mantle transition zone.

Probably the most interesting observation is that [001] glide is the dominant deformation mechanism in forsterite aggregates under our experimental conditions. As this behaviour seems not to result from high stresses or from

the presence of water, we are led to propose a possible influence of pressure. The present work provides the first evidence that [001] glide might dominate at pressures and temperatures corresponding to the lowermost upper mantle. This is likely to have important implications for the rheology of olivine as it will result in very anisotropic plastic behaviour. More work is needed however to better constrain the dominant deformation mechanisms of olivine as a function of pressure, temperature and oxygen fugacity in well-constrained experiments such as those that can be performed in the newly developed D-DIA apparatus (Wang *et al*., 2003). In parallel, it is necessary to develop a better understanding of the detailed influence of these parameters on dislocation core fine structures in olivine.

Acknowledgments: One of us (HC) was supported by the Visiting Scientists Program of the Bayerisches Geoinstitut and by the EU-program "Marie Curie Host Fellowship/ Training Sites" (Contract No HPMT-CT-2001-00231). Financial support of the French-Bavarian cooperation program (CCUFB-BFHZ) to HC and PC is gratefully acknowledged. TU is grateful to the Hungarian National Science Foundation for supporting this work under contract No OTKA-T043247. We wish to thank H. Schulze for his invaluable assistance in the samples preparation.

References

Adams, B.L., Wright, S.I., Kunze, K. (1993): Orientation imaging: The emergence of a new microscopy. *Metall. Trans*., **24A**, 819-833.

Ando, J., Irifune, T., Takeshita, T., Fujino, K. (1997): Evaluation of the non-hydrostatic stress produced in a multi-anvil high pressure apparatus. *Phys. Chem. Miner*., **24**, 139-148.

Bai, Q. & Kohlstedt, D.L. (1992a): High-temperature creep of olivine single crystals 2. Dislocation structures. *Tectonophysics*, **206**, 1-29.

—, — (1992b): High-temperature creep of olivine single crystals 3. Mechanical results for unbuffered samples and creep mechanisms. *Phil. Mag. A*, **66**, 1149-1181.

—, — (1993): Effects of chemical environment on the solubility and incorporation mechanism for hydrogen in olivine. *Phys. Chem. Miner.*, **19**, 460-471.

Bai, Q., Mackwell, S.J., Kohlstedt, D.L. (1991): High-temperature creep of olivine single crystals 1. Mechanical results for buffered samples. *J. Geophys. Res*., **96**, 2441-2463.

Blacic, J.D. & Christie, J.M. (1973): Dislocation substructure in experimentally deformed olivine. *Contrib. Mineral. Petrol*., **42**, 141-146.

Blake, B.J. (1976): An experimental investigation of dislocation glide in olivine. Massachusetts Institute of Technology, Cambridge, MA.

Bussod, G.Y., Katsura, T., Rubie, D.C. (1993): The large volume multi-anvil press as a high P-T deformation apparatus. *Pure Appl. Geophys*., **141**, 579-599.

Bretheau, T., Castaing, J., Rabier, J., Veyssière, P. (1979): Mouvement des dislocations et placticité à haute température des oxydes binaires et ternaires. *Advances in Physics*, **28**, 835-1014.

Bystricky, M., Kunze, K., Burlini, L., Burg, J.P. (2000): High shear strain of olivine aggregates: Rheological and seismic consequences. *Science*, **290**, 1564-1567.

Chen, J.H., Inoue, T., Weidner, D.J., Wu, Y.J., Vaughan, M.T. (1998): Strength and water weakening of mantle minerals, olivine, wadsleyite and ringwoodite. *Geophys. Res. Lett*., **25**, 575-578.

Chopra, P.N. & Paterson, M.S. (1981): The experimental deformation of dunite. *Tectonophysics*, **78**, 453-473.

—, — (1984): The role of water in the deformation of dunite. *J. Geophys. Res*., **89**, 7861-7876.

Cordier, P. & Rubie, D.C. (2001): Plastic deformation of minerals under extreme pressure using a multi-anvil apparatus. *Mater. Sci. Eng. A Struct. Mater.*, **309**, 38-43.

Darot, M. (1980): Déformation expérimentale de l'olivine et de la forsterite. Université de Nantes, Nantes.

Darot, M. & Gueguen, Y. (1981): High-temperature creep of forsterite single crystals. *J. Geophys. Res*., **86**, 6219-6234.

Dingley, D. (1984): Diffraction from sub-micron areas using electron backscattering in a scanning electron microscope. S*canning Electron Microsc.*, **II**, 569-575.

Dragomir, I.C. & Ungár, T. (2002): Contrast factors of dislocations in the hexagonal crystal system. *J. Appl. Cryst*., **35**, 556-564.

Dupas, C., Doukhan, N., Doukhan, J.C., Green II, H.W., Young, T.E. (1994): Analytical electron microscopy of a synthetic peridotite experimentally deformed in the β olivine stability field. *J. Geophys. Res*., **99**, 15821-15832.

Dupas-Bruzek, C., Sharp, T.G., Rubie, D.C., Durham, W.B. (1998): Mechanisms of transformation and deformation in $Mg_{1.8}Fe_{0.2}SiO_4$ olivine and wadsleyite under non-hydrostatic stress. *Phys. Earth Planet. Interiors*, **108**, 33-48.

Durham, W.B. & Goetze, C. (1977a): A comparison of the creep, properties of pure forsterite and iron-bearing olivine. *Tectonophysics*, **40**, T15-T18.

—, — (1977b): Plastic flow of oriented single crystals of olivine. 1. Mechanical Data. *J. Geophys. Res.*, **82**, 5737-5753.

Fujimura, A., Endo, S., Kato, M., Kumazawa, M. (1981): Preferred orientation of beta-Mn_2GeO_4. Seismological Society of Japan, p. 185.

Hinds, W.C. (1982): "Aerosol Technology: Properties, behavior and measurement of airbone particles". Wiley, NewYork.

Hirth, G. & Kohlstedt, D.L. (1995a): Experimental constraints on the dynamics of the partially molten upper mantle. Diffusion in the diffusion creep regime. *J. Geophys. Res*., **100**, 1981-2001.

—, — (1995b): Experimental constraints on the dynamics of the partially molten upper mantle. Diffusion in the dislocation creep regime. *J. Geophys. Res*., **100**, 15441-15449.

Jung, H.Y. & Karato, S. (2001): Water-induced fabric transitions in olivine. S*cience*, **293**, 1460-1463.

Karato, S. & Rubie, D.C. (1997): Toward an experimental study of deep mantle rheology: A new multianvil sample assembly for deformation studies under high pressures and temperatures. *J. Geophys. Res. Solid Earth*, **102**, 20111-20122.

Karato, S., Paterson, M.S., FitzGerald, J.D. (1986): Rheology of synthetic olivine aggregates: influence of grain size and water. *J. Geophys. Res*., **91**, 8151-8176.

Karato, S., Dupas-Bruzek, C., Rubie, D.C. (1998): Plastic deformation of silicate spinel under the transition-zone conditions of the Earth's mantle. *Nature*, **395**, 266-269.

Klimanek, P. & Kuzel, J.R. (1988): X-ray diffraction line broadening due to dislocations in non-cubic materials. 1. General considerations and the case of elastic isotropy applied to hexagonal crystals. *J. Appl. Cryst*., **21**, 59-66.

Kohlstedt, D.L. & Goetze, C. (1974): Low-stress high-temperature creep in olivine single crystals. *J. Geophys. Res*., **79**, 2045-2051.

Kohlstedt, D.L. & Weathers, M.S. (1980): Deformation-induced microstructures, paleopiezometers, and differential stresses in deeply eroded fault zones. *J. Geophys. Res.*, **85**, 6269-6285.

Leroux, H. (2001): Microstructural shock signatures of major minerals in meteorites. *Eur. J. Mineral*., **13**, 253-272.

Li, L., Raterron, P., Wiedner, D.J., Chen, J. (2003): Olivine flow mechanism at 8 GPa. *Phys. Earth Planet. Inter*., **138**, 113-129.

Li, L., Weidner, D., Raterron, P., Chen, J., Vaughan, M. (2004): Stress measurements of deforming olivine at high pressure. *Phys. Earth Planet. Inter*., **143-144**, 357-367.

Mackwell, S.J., Kohlstedt, D.L., Paterson, M.S. (1985): The role of water in the deformation of olivine single crystals. *J. Geophys. Res.*, **90**, 11319-11333.

Mei, S. & Kohlstedt, D.L. (2000a): Influence of water on plastic deformation of olivine aggregates 1. Diffusion creep regime. *J. Geophys. Res. Solid Earth*, **105**, 21457-21469.

—, — (2000b): Influence of water on plastic deformation of olivine aggregates 2. Dislocation creep regime *J. Geophys. Res. Solid Earth*, **105**, 21471-21481.

Nickel, K.G., Brey, G.P., Kogarko, L. (1985): Orthopyroxene-clinopyroxene equilibria in the system CaO-MgO-Al_2O_3-SiO_2 (CMAS): new experimental results and implications for two-pyroxene thermometry. *Contrib. Mineral. Petrol.*, **91**, 44-53.

Paterson, M.S. (1982): The determination of hydroxyl by infrared absorption in quartz, silicate glasses and similar materials. *Bull. Mineral.*, **105**, 20-29.

Phakey, P., Dollinger, G., Christie, J. (1972): Transmission Electron Microscopy of experimentally deformed olivine crystals. *in* "Flow and fracture of rocks", H.C. Heard, I.Y. Borg, N.L. Carter, and C.B. Raleigh, Eds. American Geophysical Union, Washington, D.C. 117-138.

Raterron, P., Wu, Y., Weidner, D.J., Chen, J. (2004): Low-temperature rheology at high-pressure. *Phys. Earth Planet. Inter*., **145**, 149-159.

Ribárik, G., Ungár, T., Gubicza, J. (2001): MWP-fit: a program for multiple whole-profile fitting of diffraction peak profiles by ab initio theoretical functions. *J. Appl. Cryst.*, **34**, 669-676.

Ribárik, G., Gubicza, J., Ungár, T. (2004): Correlation between strength and microstructure of ball milled Al-Mg alloys determined by X-ray diffraction. *Mater. Sci. Eng*. A, In press.

Sharp, T.G., Bussod, G.Y., Katsura, T. (1994): Microstructures in β-$Mg_{1.8}Fe_{0.2}SiO_4$ experimentally deformed at transition-zone conditions. *Phys. Earth Planet. Int*., **86**, 69-83.

Thurel, E. (2001): Etude en microscopie électronique en transmission des mécanismes de déformation de la wadsleyite et de la ringwoodite, p. 247. Université des Sciences et Technologies de Lille, Lille.

Thurel, E. & Cordier, P. (2003): Plastic deformation of wadsleyite: I. High-pressure deformation in compression. *Phys. Chem. Miner.*, **30**, 256-266.

Thurel, E., Cordier, P., Frost, D., Karato, S. (2003a): Plastic deformation of wadsleyite: II. High-pressure deformation in shear. *Phys. Chem. Miner*., **30**, 267-270.

Thurel, E., Douin, J., Cordier, P. (2003b): Plastic deformation of wadsleyite: III. Interpretation of dislocations and slip systems. *Phys. Chem. Miner*., **30**, 271-279.

Ungár, T. & Borbély, A. (1996): The effect of dislocation contrast on X-ray line broadening: a new approach to line profile analysis. *Appl. Phys. Lett*., **69**, 3173-3175.

Ungár, T. & Tichy, G. (1999): The effect of dislocation contrast on X-ray line profiles in untextured polycrytals. *Phy. Stat. Sol. A*, **147**, 425-434.

Ungár, T., Dragomir, I., Révész, A., Borbély, A. (1999): The contrast factor of dislocations in cubic crystals: The dislocation model of strain anisotropy in practice. *J. Appl. Cryst*., **32**, 992-1002.

Ungár, T., Gubicza, J., Ribarik, G., Borbély, A. (2001): Crystallite size distribution and dislocation structure determined by diffraction profile analysis: principles and practical application to cubic and hexagonal crystals. *J. Appl. Cryst*., **34**, 298-310.

Wang, Y.B., Durham, W.B., getting, I.C., Weidner, D.J. (2003): The deformation-DIA: A new apparatus for high temperature triaxial deformation to pressures up to 15 GPa. *Rev. Sci. Instr*., **74**, 3002-3011.

Warren, B.E. & Averbach, B.L. (1950): The effect of cold work distortion on X-ray pattern. *J. Appl. Phys*., **21**, 595-610.

Weidner, D.J., Wang, Y., Vaughan, M.T. (1994): Yield strength at high pressure and temperature. *Geophys. Res. Let*., **21**, 753-756.

Wilkens, M. (1970): The determination of density and distribution of dislocations in deformed single crystals from broadened X-ray diffraction profiles. *Phys. Stat. Sol. A*, **2**, 359-370.

Williamson, G.K. & Hall, W.H. (1953): X-ray line broadening from filed aluminium and Wolfram. *Acta Metall*., **1**, 22-31.

Yang, L.H., Söderlind, P., Moriarty, J.A. (2001): Accurate atomistic simulation of (a/2)<111> screw dislocations and other defects in bcc tantalum. *Philos. Mag. A*, **81**, 1355.

Zhang, S.Q., Karato, S., Gerald, J.F., Faul, U.H., Zhou, Y. (2000): Simple shear deformation of olivine aggregates. *Tectonophysics*, **316**, 133-152.

Received 25 September 2003
Modified version received 17 April 2004
Accepted 15 September 2004